Bidirectional reflectance distribution function effects in ladar-based reflection tomography

Xuemin Jin* and Robert Y. Levine

Spectral Sciences, Inc., Burlington, Massachusetts 01803, USA

*Corresponding author: xjin@spectral.com

Received 19 May 2009; accepted 26 June 2009;
posted 2 July 2009 (Doc. ID 111586); published 15 July 2009

Light reflection from a surface is described by the bidirectional reflectance distribution function (BRDF). In this paper, BRDF effects in reflection tomography are studied using modeled range-resolved reflection from well-characterized geometrical surfaces. It is demonstrated that BRDF effects can cause a darkening at the interior boundary of the reconstructed surface analogous to the well-known beam hardening artifact in x-ray transmission computed tomography (CT). This artifact arises from reduced reflection at glancing incidence angles to the surface. It is shown that a purely Lambertian surface without shadowed components is perfectly reconstructed from range-resolved measurements. This result is relevant to newly fabricated carbon nanotube materials. Shadowing is shown to cause crossed streak artifacts similar to limited-angle effects in CT reconstruction. In tomographic reconstruction, these effects can overwhelm highly diffuse components in proximity to specularly reflecting elements. Diffuse components can be recovered by specialized processing, such as reducing glints via thresholded measurements.

OCIS codes: 100.3010, 100.6950, 140.3460, 240.3695, 240.5770, 240.6700.

1. Introduction

Laser radar (ladar) imaging is based on laser reflection from an object resolved in range, velocity (Doppler), or angle [1–3]. The received signal in each resolution cell is the reflected radiance from surface elements back to the ladar. A series of signals along the resolved coordinate direction produces a reflective projection of the object, and a full tomographic reconstruction of the surface is formed from many such projections at different viewing directions [4–8]. Object surface materials dictate light reflection from the surface and, therefore, have a major impact on reflected signals and the resulting reconstructed image. This paper analyzes the effects of surface materials on ladar *range-resolved* reflection tomography. The results can be extended easily to Doppler and angle–angle imaging, or a combination of resolved projected coordinates.

The magnitude and direction of reflected radiance from a surface are described by the bidirectional reflectance distribution function (BRDF) [9–13]. For a specified wavelength, it is defined as the ratio of reflected radiance in a particular direction to the irradiance incident on the surface. The BRDF is an intrinsic optical property of the surface material and texture. BRDF modeled radiance and shadowing can introduce distinct artifacts in the application of reflection tomography to the reconstruction of a surface. Diffuse and specular reflection lobes give rise to a reduction of reflected radiance back to the ladar from glancing surface incidence that leads to an anomalous reconstruction similar to the beam hardening artifact in x-ray computed tomography (CT) [14–18]. Through modeling and simulation in this paper, the effect is shown to amplify as the surface becomes less Lambertian. As noted in Ref. [8], shadowing in reflection tomography creates artifacts similar to the limited-angle distortion in transmission CT [19–23]. This effect is also demonstrated in this paper for realistic surface materials. However, it is the combination of diffuse and specular

0003-6935/09/214191-10$15.00/0

shadowed surfaces that has the strongest BRDF effect on the overall reconstruction. We show with a disk pair phantom that the placement of specular elements near diffuse elements can have the effect of completely removing the diffuse element from the reconstruction. Apparently, limited-angle artifacts can dominate the reconstruction of the diffuse component because the specular component is shadowed by the diffuse component. While BRDF effects have been considered in reflection tomography [8], further isolating and characterizing distinct BRDF-based artifacts is a useful advance. Previously developed CT artifact mitigation algorithms for beam hardening [15–18] and limited-angle distortion [19–21] may be applied to reflection tomography.

As with the classic Shepp–Logan phantom in transmission CT [24], the analysis of well-characterized phantoms for reflection tomography aids in the assessment of artifacts and reconstruction algorithms. In this paper we consider three phantoms of increasing complexity: the disk, the ellipse, and adjacent disk pairs. The ellipse is distinguished from the disk in that, at oblique incidence, there are range bins in which radiance is reflected from one side of the phantom adjacent to bins in which radiance is reflected from both sides. This results in angularly asymmetric reconstruction artifacts. The adjacent disk pair is slightly more complex in that there are range bins without any radiance—gaps appear in the range profiled radiance due to shadowing. Additionally, we are able to assign different materials to shadowed disks to assess the effects of proximate disparate surfaces in the overall reconstruction.

Depending on the application, there are a variety of BRDF models in the literature [10–13]. In this paper, we use the Sandford–Robertson (SR) BRDF model, which was developed by the Air Force to characterize aircraft paints and coatings and is accurate across typical ladar bands in the range of 0.5–12 μm [10]. As is typical with many models, the SR BRDF separately parameterizes diffuse and specular reflections —a convenient distinction for characterizing artifacts in reflection tomography. It should be emphasized that the identity and character of reconstruction artifacts are independent of the BRDF model used to describe the surface.

The rest of this paper is organized as follows. In Section 2 we present a brief review of the BRDF definition. The coupling of the BRDF model with a description of range-resolved ladar measurements of a two-dimensional surface is contained in Section 3. An "offset surface" formalism for ladar measured radiance is introduced to mathematically characterize surface reconstruction, and to demonstrate BRDF effects. It is shown that a Lambertian surface is fully reconstructed with ladar-based tomography. This result is directly applicable to the recently invented carbon nanotube materials [25,26]. In Section 4, using the two-dimensional surface model, a series of simulations highlight reconstruction artifacts due to non-Lambertian BRDF lobes and shadowing with the disk, ellipse, and disk pair phantoms. A conclusion follows in Section 5. Details of the SR BRDF model used in the simulations and analyses are provided in Appendix A.

2. Bidirectional Reflectance Distribution Function Model

The BRDF was first introduced by Nicodemus [9]. The function describes the ratio of reflected radiance exiting the surface into a solid angle $d\omega_r$ to the irradiance incident on the surface from a solid angle $d\omega_i$, where both incident and reflected solid angles originate at the surface point of reflection. For a reflected radiance $dL_r(\lambda;\theta_r,\phi_r)$ from incident radiance $L_i(\lambda;\theta_i,\phi_i)$, the BRDF is defined as [9]

$$F(\lambda;\theta_i,\phi_i;\theta_r,\phi_r)=\frac{dL_r(\lambda;\theta_r,\phi_r)}{L_i(\lambda;\theta_i,\phi_i)\cos\theta_i d\omega_i}, \tag{1}$$

with incident and reflected polar and azimuthal angles (θ_i,ϕ_i) and (θ_r,ϕ_r), and for light wavelength λ. The important factor $(\cos\theta_i)^{-1}$ normalizes an incident collimated radiance by the projected area at the reflection point in order to obtain a function F that is *locally* intrinsic to the surface.

The directional reflectivity is defined as the integration of the BRDF over the hemisphere above the reflecting surface:

$$\rho(\lambda;\theta_i,\phi_i)=\int_0^{\pi/2}\mathrm{d}\theta_r\sin\theta_r\int_0^{2\pi}\mathrm{d}\varphi_r F(\lambda;\theta_i,\phi_i;\theta_r,\phi_r)\cos\theta_r. \tag{2}$$

For a graybody surface in thermal equilibrium, Kirchoff's law states that the spectral absorptivity and emissivity are equal. In that case, for opaque surfaces with zero transmittance, we have by energy conservation the condition

$$\varepsilon(\lambda;\theta_i,\phi_i)+\rho(\lambda;\theta_i,\phi_i)=1, \tag{3}$$

where $\varepsilon(\lambda;\theta_i,\phi_i)$ is the directional emissivity. This condition constrains the BRDF.

In the following, we assume that the surface has no preferential marks (striae) nor surface scratches. This reduces the number of dependent angles in F to three: θ_i, θ_r, and $(\phi_r-\phi_i)$. Furthermore, the properties of ladar-based reflection tomography considered in this paper are sufficiently described by two-dimensional reconstructions in the plane of incidence. The azimuthal dependence of the BRDF is irrelevant in this case.

In this paper we use the SR [10] BRDF model to characterize BRDF effects in ladar-based reflection tomography. This model provides a consistent description of surface emissive and reflectance properties for a large number of coatings [11]. It contains diffuse and specular reflection:

$$F(\lambda;\theta_i,\theta_r)=F_d(\lambda;\theta_i,\theta_r)+F_s(\lambda;\theta_i,\theta_r), \tag{4}$$

which is a convenient characterization for isolating reconstruction artifacts. Details of the SR model are given in Appendix A for reference. The diffuse reflectance lobe is defined in terms of an angle independent diffuse reflectivity $\rho_d(\lambda)$, and lobe shape parameter $b \in [0,1]$. The specular reflectance lobe is written in terms of an *angle dependent* specular reflectivity $\rho_s(\lambda;\theta_i)$ and a specular lobe shape parameter e. As shown in Appendix A, the expression in Eq. (3) connects ρ_s to measurable diffuse reflectance $\rho_d(\lambda)$ and emissivity $\varepsilon(\lambda,\theta_i)$. An empirically validated assumption in the SR model is that both b and e are wavelength independent. The model contains four semiempirical parameters, two each for diffuse and specular reflection, that are derived from analysis of reflectance data. A review of the BRDF models can be found in Ref. [12].

3. Coupled BRDF and Range-Resolved Ladar Signature

In this section uniform illumination of a reflecting two-dimensional surface with a range-resolved ladar is described analytically. Consider the two-dimensional surface $y = f(x)$ in Fig. 1 and a uniform ladar beam incident from the $+y$ direction. By timing the returned signal, the ladar assigns reflected radiance to a range bin of width dy as shown in Fig. 1. The surface normal at x is given by

$$\boldsymbol{n} = \frac{1}{\sqrt{1+f'(x)^2}}[-f'(x)\boldsymbol{x} + \boldsymbol{y}], \tag{5}$$

and the surface elements by

$$dl = \sqrt{dx^2 + dy^2} = dy\frac{\sqrt{1+f'(x)^2}}{|f'(x)|}. \tag{6}$$

The radiance reflected into the range bin at y is proportional to the sum of those arc lengths dl that intersect the range bin interior; each weighted by $\cos(\theta)$ to project transversely to the beam direction and by the appropriate BRDF $F(\lambda;\theta;-\theta)$ for a ladar angle of incidence θ to the surface location (x,y). Evaluating $F(\lambda;\theta_i;\theta_r)$ with $\theta_r = -\theta_i$ corresponds to the assumption that the ladar receiver is colocated with the transmitter at a remote range. For convenience we will assume $\theta_r = -\theta_i$ for the rest of this paper.

From Fig. 1 and Eq. 5, it is seen that the incidence angle satisfies

$$\boldsymbol{n}\cdot\boldsymbol{y} = \cos(\theta) = 1/\sqrt{1+f'(x)^2}, \tag{7}$$

so that from Eq. (6) the binned radiance is proportional to

$$dl\cos(\theta)\times F(\lambda;\theta;-\theta) = \frac{dy}{|f'(x)|}\times F(\lambda;\theta;-\theta). \tag{8}$$

Note that a constant (θ-independent) BRDF corresponds to a Lambertian surface and the reflected radiance is proportional to only the projection of the arc length onto the ladar line of sight (LOS).

Consider the two surfaces defined in Fig. 2. Surface #1 is parameterized from the origin by the vector $(x,f(x))$ and surface #2 is given by $(x,f(x)-\Delta(x))$, where Δ is the offset of surface #2 from surface #1. Taking the difference $(f(x)-y)$ shown in Fig. 2, we have the result that the binned area element is given by

$$(f(x)-y)dx = \Delta(x)dx = \Delta(x)\frac{dy}{|f'(x)|}. \tag{9}$$

From Eqs. (8) and (9) the surface offset is dependent on the BRDF through the relation

$$\Delta(x) = F(\lambda,\theta;-\theta), \tag{10}$$

where the x dependence on the right-hand side of Eq. (10) is implicit in θ. Therefore, from Eq. (8), the effect of ladar ranging is to measure the BRDF-weighted area between the surface and an offset surface. For a Lambertian surface, $F(\lambda,\theta,-\theta)$ is θ independent, implying a constant offset in the ladar beam direction, which is intuitively appropriate for surface reconstruction. In general, even without shadowing, the BRDF has a significant impact on the actual reconstructed surface because of its dependence on the angle between the incident and surface normal directions. In particular, the reduction at glancing angles has the effect of lessening that view's contribution to the final reconstruction and is the

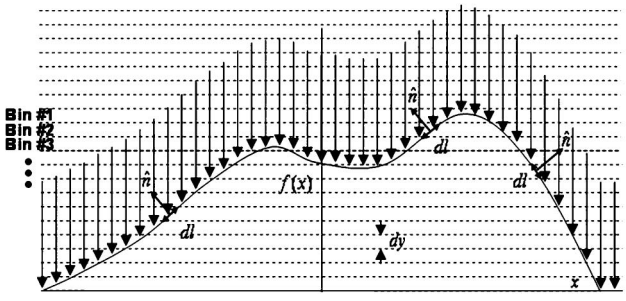

Fig. 1. Geometry for ladar-based ranging and surface reconstruction.

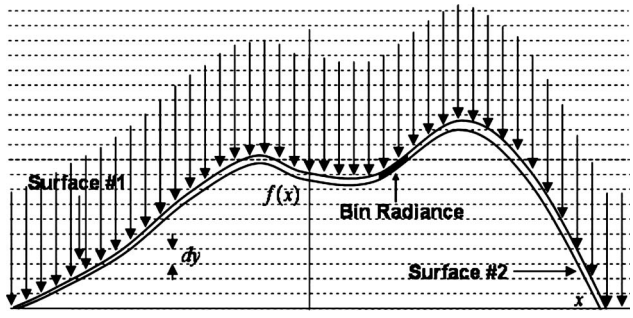

Fig. 2. Reconstructed region: area between surface #1 and surface #2.

source of the edge darkening artifact described in Subsection 4.A.

4. BRDF Effects in Reconstructed Reflection Phantoms

In this section the binned, range-resolved ladar signature defined in Section 3 is used to characterize BRDF effects in reflection tomography. For the BRDF, $F(\lambda, \theta, -\theta)$ in Eq. (8), we use the SR model defined in Appendix A. As with the case of transmission CT [24], reconstruction phantoms specific to reflection tomography are critical in order to assess artifacts. Because it is possible to derive analytical results for simple geometric shapes, the modeled reflection from these phantoms does not contain false artifacts from a faceted representation of the surface. Three two-dimensional phantoms are considered. The simplest shape, a disk, has symmetric reflections from each side so that pure BRDF artifacts can easily be isolated from shape effects (such as shadowing). An elliptical disk is shown in Fig. 3 to have views in which asymmetrical shadowing causes asymmetries in the range profiles. The third level of complexity, two adjacent disks in Fig. 4, has gaps in the binned radiance due to the shadowing of each disk by the other.

For all tomographic reconstructions in this paper, a standard filtered backprojection algorithm is adopted with 360 1° incremented views covering the entire angular domain [27,28]. Projection and backprojection ray tracing required for forward simulation of reflected radiance and reconstruction are performed using the Siddon algorithm [29]. It is assumed that the incident ladar beam is uniform, covers the target, and the ladar receiver is at the same location as the transmitter ($\theta_r = -\theta_i; \phi_r = \phi_i$).

A. BRDF Glancing Incidence Artifact

The key feature of BRDF reflection embodied in the SR model in Eqs. (A1) and (A2) are radiance lobes centered on the surface normal for diffuse reflection and on the glint vector for specular reflection. In either case, there is a significant reduction in the reflected radiance at glancing incidence, which introduces a distinctive artifact in the tomographic reconstruction of the surface.

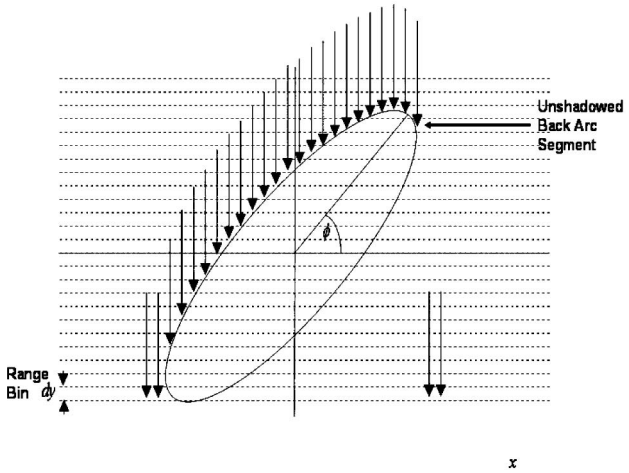

Fig. 3. Ladar-based radiance bins for an elliptical phantom. Location of radiance asymmetry indicated.

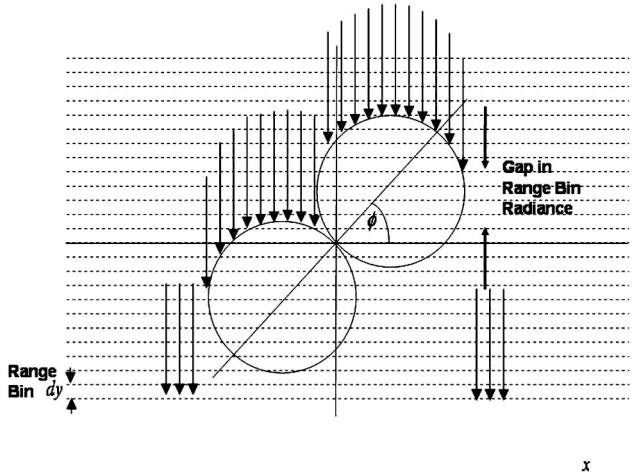

Fig. 4. Ladar-based radiance bins for adjacent disks phantom. Location of radiance gap indicated.

To characterize the BRDF effect arising from diffuse reflection, we set the specular term in Eq. (4) to zero and consider a *diffusely* coated two-dimensional disk of radius A in which the binned radiance is independent of viewing angle. Assuming a ladar range bin resolution of $A/256$, the binned radiance is computed using Eqs. (A1) and (A2) with $\theta_r = -\theta_i$ for every binned surface element. A diffuse spectral reflectivity $\rho_d(\lambda) = 1.0$ is assumed.

The resulting range profile, received radiance versus bin number, is shown in Fig. 5 for two grazing reflectivities $b = 0$ (Lambertian) and $b = 0.99$ (narrowly reflective). As b increases, the radiance is larger at the disk center (bin closest to the ladar) relative to the bins crossing near the disk periphery;

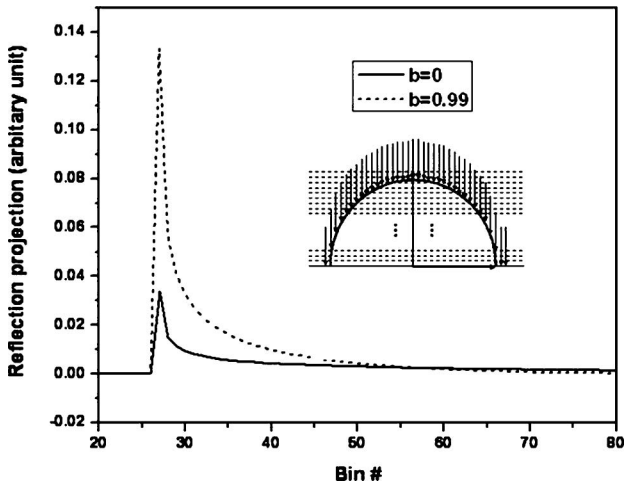

Fig. 5. Ladar range-resolved radiance for a two-dimensional disk of radius A with $A/256$ bin resolution, and grazing surface reflectivities $b = 0$ (solid curve) and $b = 0.99$ (dotted curve) in the diffuse SR BRDF model in Eq. (A1). Inset: disk illumination geometry. Note that the lower half of the disk is shadowed by the upper half.

as expected due to Eq. (A1) with large grazing $\theta_r \cong \pi/2$. While $b = 0$ and $b = 0.99$ are not typical with standard materials, the recent invention of very black carbon nanotube surfaces highlights emerging new extreme BRDF properties in materials [25,26].

The 360 view reconstructed images using the range profiles in Fig. 5 are shown in Figs. 6(a) and 6(b) for $b = 0$ and $b = 0.99$, respectively. Slices through the reconstructed image centers are shown in Fig. 6(c). As proven in Section 3, the Lambertian ($b = 0$) surface is perfectly reconstructed. Note, however, for a nonzero b value, there is a "darkening" effect near the surface interior—reconstructed values are decreasing and becoming negative toward the interior boundary of the surface. The effect is strikingly similar, but of the opposite sign, to the well-known cupping artifact due to beam hardening in x-ray transmission tomography [16]. In x-ray CT, the lesser energy (softer) beam on a peripheral ray backprojects to higher attenuation than the higher energy (harder) beam that traverses more material in the center of the disk. Analogously, in reflection tomography, the relative reduction of binned radiance at the glancing incidence on the target periphery backprojects to at darker surface element.

As shown in Fig. 3, ladar range profiles are view dependent for a two-dimensional elliptical surface due to asymmetric shadowing. For an elliptical surface with semimajor axis $A = 0.6$ and semiminor axis $B = 0.3$, we computed the binned radiance using Eqs. (A1) and (A2) for 360 views. The reconstructed images in Figs. 7(a) and 7(b) correspond to $b = 0$ (Lambertian) and $b = 0.99$, respectively. As expected, the boundary darkening is concentrated at the tapered ends of the ellipse where there is more radiance loss due to oblique incidence.

We now consider specular reflection, and set the diffuse term in Eq. (4) to zero. Because of a generally narrower reflectance lobe centered at the Snell's law reflectance angle, specular reflection has a greater reduction of reflected radiation for glancing incidence. Figures 8(a) and 8(b) contain 360 view reconstructions of two-dimensional disks with SR glint lobe eccentricities $e = 1.0$ and $e = 0.007$, respectively. The latter corresponds to significant glinting surfaces, such as with commercial aluminum. At each binned surface element, the reflected radiance was determined by Eqs. (A5) and (A6) with $\rho_s(\lambda, \theta) = 1.0$, which corresponds to pure specular reflection at the surface ($\varepsilon = 0$, $\rho_d = 0$). As seen in Fig. 8(a), if there is no glint lobe ($e = 1.0$); the surface is perfectly reconstructed. In the case of significant glinting ($e = 0.007$) in Fig. 8(b), a deep narrow darkening is seen in the interior boundary of the surface attributed to reduced reflection at oblique angles of incidence. Because a glint lobe falls off more sharply than a diffusive reflectance lobe, it is seen by the comparison of Figs. 6(b) and 8(b) that the glint artifact is sharper than the diffuse reflection artifact.

B. BRDF and Shadowing Effects

In Subsection 4.A BRDF artifacts in reflection tomography are demonstrated that are analogous to transmission CT beam hardening. In this subsection, multicomponent shadowing is shown to cause artifacts similar to the crossed streak patterns of limited-angle CT, which occur when the set of view directions do not fully cover the 180° range around the object [19,21].

Phantoms consisting of two adjacent disks, as in Fig. 4, provide a tractable model of component shadowing. A full 360 view reconstruction of two adjacent disks of radii 0.4 and 0.3 was performed assuming real surface coatings that have been fit to a *full* SR diffuse and specular BRDF model. The diffuse coating is dark gray with $\lambda = 1.0\,\mu$m and SR parameters given by $\rho_d(1\,\mu\text{m}) = 0.032$, $\varepsilon(1\,\mu\text{m}) = 0.877$, $b = 0.1$, and $e = 0.17$. The specular coating is a commercial aluminum surface with $\lambda = 1.0\,\mu$m and SR parameters given by $\rho_d(1\,\mu\text{m}) = 0.047$, $\varepsilon(1\,\mu\text{m}) = 0.53$, $b = 0.1$, and $e = 0.007$. As shown in Figs. 9(a) and 9(b), for both diffuse gray and specular aluminum coatings, the two disks are reconstructed with the subsurface darkening described in Subsection 4.A. In addition, for both coatings, there is a crossed pattern artifact similar to the limited-angle reconstruction in transmission CT reconstruction. The cross pattern is the point-spread function of a limited-angle reconstruction [19], which in Fig. 9 is summed over the surface pixels. As noted in Fig. 4, gaps occur in the

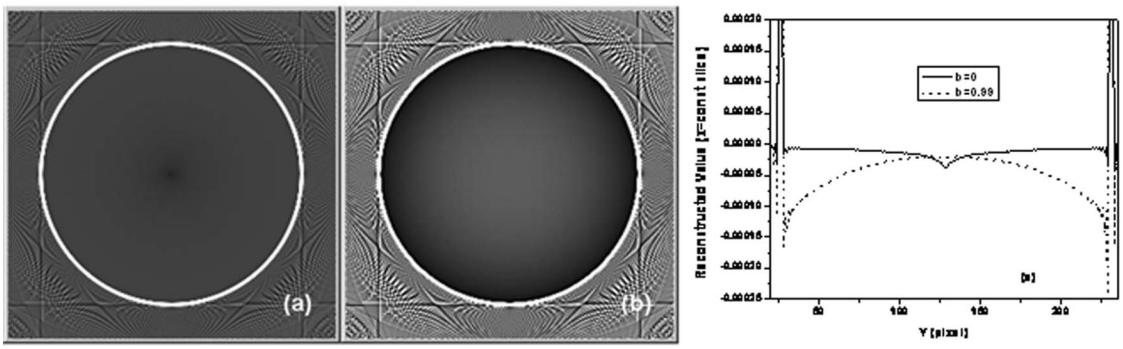

Fig. 6. Tomographic reconstruction of a disk with $A/256$ resolved range bins for disk radius $A = 0.8$ using the diffuse SR BRDF model in Eq. (A1). (a) $b = 0$ Lambertian, (b) $b = 0.99$ narrowly reflective, and (c) slices through the center of the reconstructions for $b = 0$ (solid curve) and $b = 0.99$ (dotted curve). The dip in the center of (a) is a sampling artifact.

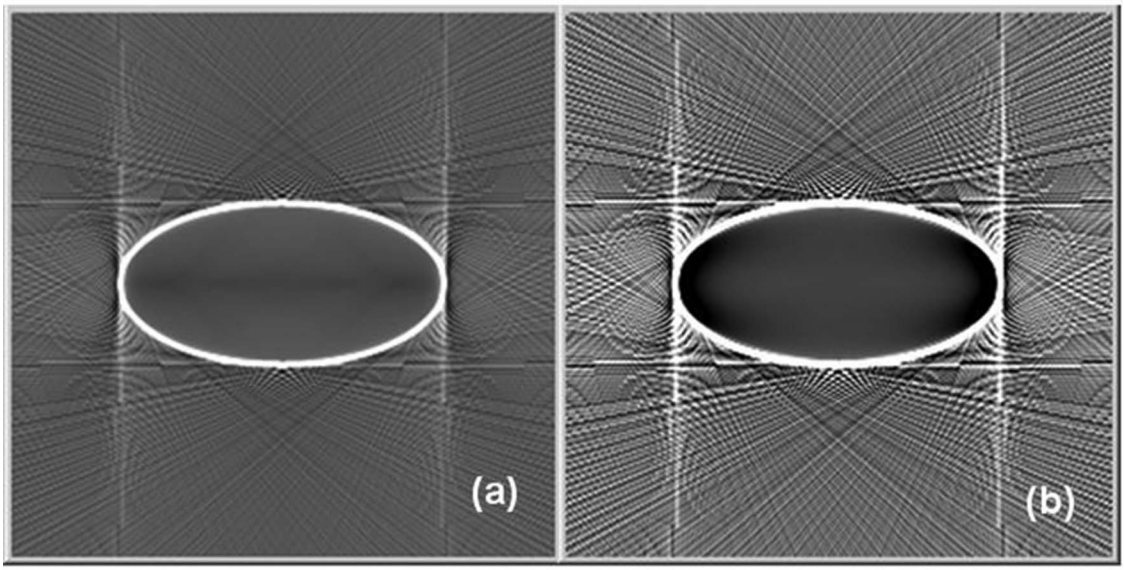

Fig. 7. Tomographic reconstructions of an elliptical disk with semimajor axis $A = 0.6$ and semiminor axis $B = 0.3$. Input data are range-resolved ladar returned radiance computed using the SR diffuse BRDF model in Eq. (A1) with (a) $b = 0$, (b) $b = 0.99$.

radiance range profiles due to *component shadowing* effects. The shadowing gaps are equivalent to missing views in the angular domain.

It is interesting to consider different coatings on the two disks in the adjacent disk pair phantom. Figure 10 shows the 360 view reconstructions for the adjacent disk pair phantom with (a) a dark gray larger disk and a specular aluminum small disk, and (b) a specular aluminum large disk and a dark gray small disk. The SR BRDF parameters at $\lambda = 1.0\,\mu$m for these coatings are given above. It is a remarkable feature of the reconstructions in Fig. 10 that the dark gray disks are virtually invisible. The reason is that the range-resolved reflected radiance is dominated by the specular coated component, and this component is shadowed by the diffuse component. The resulting limited-angle artifacts mask the diffuse component reconstruction.

Integral to the distortion in the Fig. 10 reconstructions is the fact that glints are much more intense than the underlying diffuse reflection. Consequently, the diffuse component is not discernable due to specular reconstruction artifacts. The diffuse component can be recovered by reducing this disparity in binned reflected radiance. Figure 11(a) contains the adjacent disk pair reconstruction corresponding to Fig. 10(a), but with the logarithm of the binned radiance as input. The diffuse lobe on the left side is observable. In Fig. 11(b), the binned reflected radiance is clipped at a threshold of 0.008 times the maximum

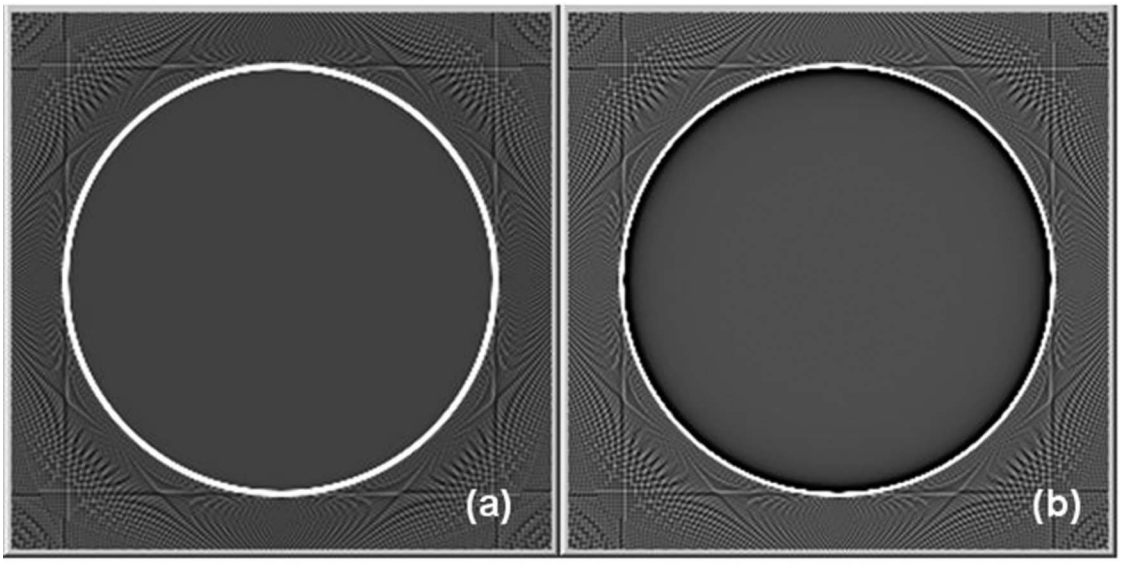

Fig. 8. Tomographic reconstruction of a disk using ladar range-resolved radiance with the specular SR BRDF model in Eq. (A5) with (a) $e = 1$, (b) $e = 0.007$.

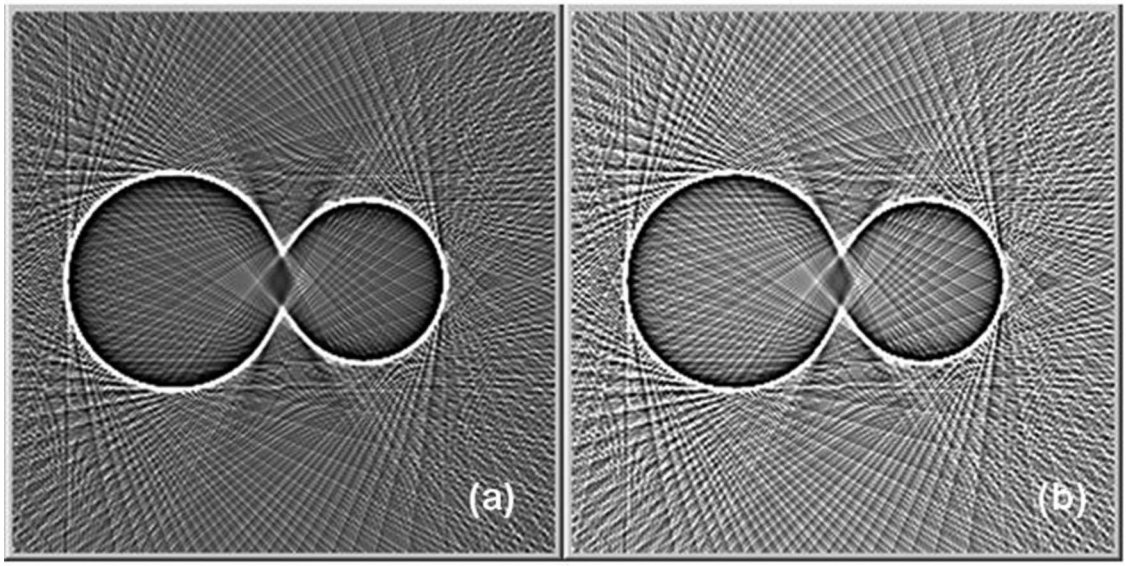

Fig. 9. Tomographic reconstruction of two adjacent disk phantoms with radii 0.4 and 0.3 from range-resolved ladar reflection with the full SR BRDF model in Eqs. (A1)–(A8): (a) dark gray coatings on both disks, (b) commercial aluminum coatings on both disks.

value. The diffuse and specular disks are simultaneously reconstructed in this case with minimal distortion.

5. Summary and Conclusions

Reflection tomography artifacts arising from surface BRDF effects are considered in a series of reconstruction phantoms of increasing shadowing complexity. The surfaces are sufficiently tractable so that range-resolved ladar radiance can be analytically determined to avoid faceting effects in reconstruction simulations. Using the well-tested SR BRDF model for coatings, two types of artifacts are demonstrated on the phantoms. The relative lessening of reflected radiance at glancing angles in both the diffuse and specular reflection lobes is shown to cause a darkening at the interior boundaries of the reconstructed surfaces. It is suggested that this BRDF artifact in reflection tomography is similar, but of opposite sign, to the well-known beam hardening artifact in x-ray transmission CT. Furthermore, using an adjacent disk phantom, it is demonstrated that component shadowing results in crossed streaked artifacts analogous to the limited-angle distortion in x-ray CT. It is shown that BRDF effects are more significant in this type of distortion if a diffuse component is adjacent to a specularly coated component. Artifacts from the shadowed glinty surfaces appear

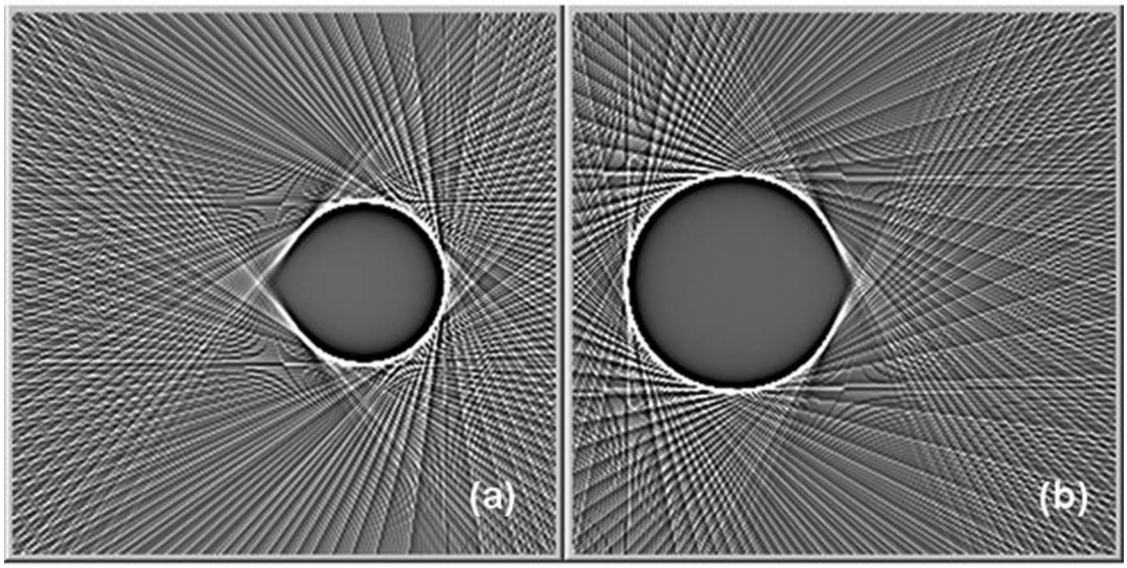

Fig. 10. Tomographic reconstruction of two adjacent disks with radii 0.4 and 0.3 from range-resolved ladar reflection with the full SR BRDF model in Eqs. (A1)–(A8): (a) dark gray coating on the large disk and commercial aluminum surface on the small disk, (b) commercial aluminum surface on the large disk and dark gray coating on the small disk.

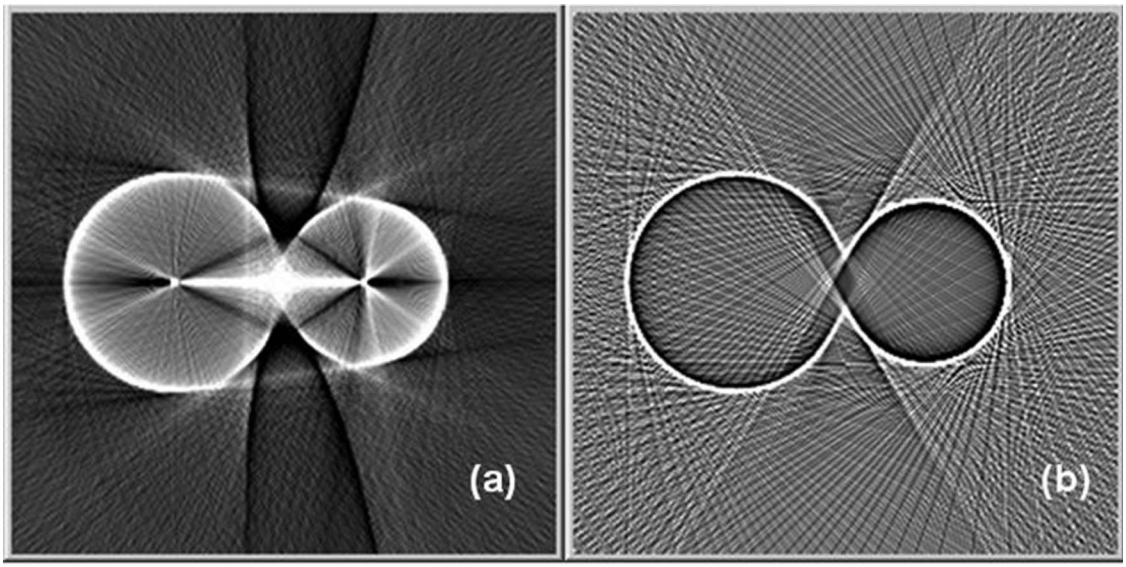

Fig. 11. Tomographic reconstruction of two adjacent disks in Fig. 10(a) with the full SR BRDF model in Eqs. (A1)–(A8): (a) input logarithm of the binned radiance, (b) clipped radiance to remove glints at a threshold of 0.008 times the maximum value.

across the entire reconstructed images to mask the diffuse component. The missing diffuse components can be recovered by thresholding the binned radiance to remove glints.

With relatively few coatings and a moderate amount of shadowing, it may be possible to determine the parameters in the component BRDF models from ladar measurements. However, a geometric surface reconstruction is required for this task in order to isolate binned radiances to particular components at different views. That reconstruction is possible by removing limited-angle artifacts from highly specular components. We are currently pursuing this direction of research as an application of the characterization of reconstruction artifacts discussed in this paper.

Appendix A

In this appendix we define the diffuse and specular components in the SR BRDF model [10]. The diffuse component, $F_d(\lambda;\theta_i,\theta_r)$, is assumed to be an average property of the surface resulting from subsurface scattering and from multiple scattering due to surface roughness on the microscopic level. The diffuse component is modeled as

$$F_d(\lambda;\theta_i,\phi_i;\theta_r,\phi_r)=\frac{g(\theta_i)\rho_d(\lambda)g(\theta_r)}{\pi G(b)^2}, \tag{A1}$$

where $\rho_d(\lambda)$ is the diffuse spectral reflectivity and

$$g(\theta)=\frac{1}{1+b^2\tan^2\theta} \tag{A2}$$

is an angular form factor describing the shape of the diffuse reflection lobe. The parameter b is defined to be the grazing angle reflectivity, and is determined from the surface reflectance data. For a perfectly diffuse (Lambertian) surface with $b=0$, radiance is reflected isotropically—reflected radiance measured in any direction is the same for a given incident ray. The factor $(\pi G(b)^2)^{-1}$ in Eq. (A1) normalizes the integrated reflected radiance to $\rho_d(\lambda)$

$$\begin{aligned}G(b)&=\frac{1}{\pi}\int_0^{\pi/2}\mathrm{d}\theta_i\sin\theta_i\int_0^{2\pi}\mathrm{d}\phi_i\, g(\theta_i)\cos\theta_i\\&=\frac{1}{1-b^2}\left[1+\frac{b^2}{1-b^2}\ln(b^2)\right].\end{aligned} \tag{A3}$$

Integration of Eq. (A1) over all observer angles yields the directional diffuse reflectance lobe

$$\rho_d(\lambda;\theta_i,\phi_i)=\frac{g(\theta_i)}{G(b)}\rho_d(\lambda). \tag{A4}$$

The SR specular component $F_s(\lambda;\theta_i,\theta_r)$ is based on the work of Trowbridge and Reitz [30], who describe the rough surface reflection using an elliptical lobe with eccentricity e. The specular component is given by

$$F_s(\lambda;\theta_i,\phi_i;\theta_r,\phi_r)=\frac{1}{4\pi}\rho_s(\lambda,\theta_i)\frac{h(\alpha)}{H(\theta_i)\cos\theta_r}, \tag{A5}$$

where α is the glint angle shown in Fig. 12, $\rho_s(\lambda,\theta)$ is the directional specular reflectivity, e is the specularity parameter describing the specular lobe as

$$h(\alpha)=\frac{1}{(e^2\cos^2\alpha+\sin^2\alpha)^2}, \tag{A6}$$

and $H(\theta_i)$ is a normalization factor. The glint angle is defined as the direction of the glint vector $\boldsymbol{g}$ that bisects the incident and reflected light directions. As seen in Fig. 12, the parameterization in Eqs. (A5)

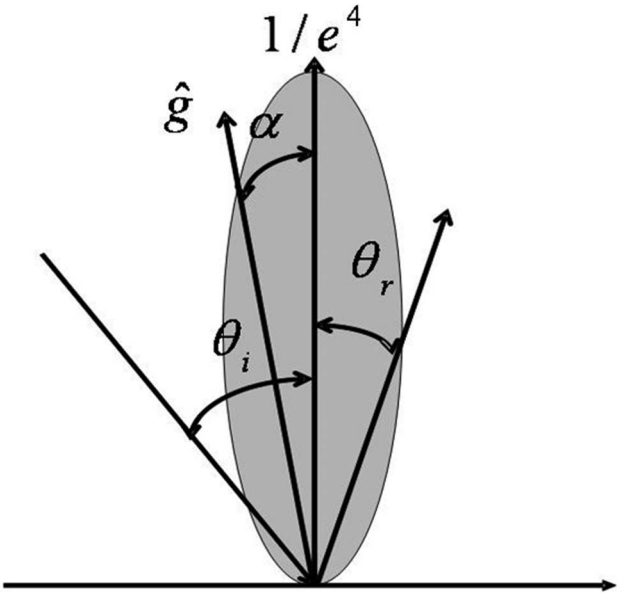

Fig. 12. Sandford–Robertson model: specular reflection lobe showing glint angle α defined as the direction of the glint vector $\mathbf{g}$. Weighting function $h(\alpha)$ shown in shade.

and (A6) suggest a $1/e^4$ weighting of the reflectance towards Snell's law at $\alpha = 0$ so that extremely small e values correspond to highly specular (mirrorlike) reflection.

The directional specular reflectivity in Eq. (A5) is determined from Eq. (3) by assuming that the directional emissivity has the same angular dependence as the diffuse reflectance $\rho_d(\lambda, \theta_i)$ in Eq. (A4):

$$\varepsilon(\lambda, \theta) = \varepsilon(\lambda) \frac{g(\theta)}{G(b)}. \tag{A7}$$

From Eqs. (3), (A4), and (A7), we have the specular reflectivity

$$\rho_s(\lambda, \theta_i) = 1 - \frac{[\varepsilon(\lambda) + \rho_d(\lambda)] g(\theta_i)}{G(b)}. \tag{A8}$$

Consistency of the specular component definition in Eq. (A5) requires

$$\rho_s(\lambda, \theta_i) = \int_0^{\pi/2} \mathrm{d}\theta_r \sin\theta_r \int_0^{2\pi} \mathrm{d}\phi_r \, F_s \cos\theta_r, \tag{A9}$$

with the resulting normalization factor

$$H(\theta_i) = \frac{1}{4\pi} \int_0^{\pi/2} \mathrm{d}\theta_r \sin\theta_r \int_0^{2\pi} \mathrm{d}\varphi_r \, h(\alpha) \frac{1}{2e^2} \times \left\{ (1-e^2)\cos\theta_i + \frac{(2e^2 + (1-e^2)^2 \cos^2\theta_i)}{\sqrt{4e^2 + (1-e^2)^2 \cos^2\theta_i}} \right\}. \tag{A10}$$

The SR BRDF model is completely characterized by four parameters: the diffuse spectral reflectance $\rho_d(\lambda)$ and grazing angle reflectivity b in Eqs. (A1)–(A4), and the spectral emissivity $\varepsilon(\lambda)$ and the specularity parameter e in Eqs. (A7)–(A10). It is noted that, empirically, the lobe parameters e and b are insensitive to wavelength across typical ladar visible-to-thermal IR bands.

References

1. F. K. Knight, D. L. Klick, D. P. Ryan-Howard, and J. R. Theriault, "Visible laser radar: range tomography and angle-angle-range," Opt. Eng. **30**, 55–65 (1991).
2. R. M. Marino, T. Stephens, R. E. Hatch, J. L. McLaughlin, J. G. Mooney, M. E. O'Brian, G. S. Rowe, J. S. Adams, L. Skelly, R. C. Knowlton, S. E. Forman, and W. R. Davis, "A compact 3D imaging laser radar system using geiger-mode APD arrays: systems and measurements," Proc. SPIE **5086**, 1–15 (2003).
3. A. L. Kachelmyer, "Range-Doppler imaging: waveforms and receiver design," Proc. SPIE **999**, 138–161 (1988).
4. C. L. Matson, "Tomographic satellite image reconstruction using ladar E-field or intensity projections: computer simulation results," Proc. SPIE **2566**, 166–176 (1995).
5. J. K. Parker, E. B. Craig, D. I. Klick, F. K. Knight, S. R. Kulkarni, R. M. Marino, J. R. Senning, and B. K. Tussey, "Reflective tomography: images from range-resolved laser radar measurements," Appl. Opt. **27**, 2642–2643 (1988).
6. F. K. Knight, S. R. Kulkarni, R. M. Marino, and J. K. Parker, "Tomographic techniques applied to laser radar reflective measurements," Lincoln Lab. J. **2**, 143–159 (1989).
7. S. A. Hanes, V. N. Benham, J. B. Lasche, and K. B. Rowland, "Field demonstration and characterization of a 10.6 micron reflection tomography imaging system," Proc. SPIE **4167**, 230–241 (2001).
8. C. L. Matson and J. Boger, "Laboratory validation of range-resolved reflective tomography signal-to-noise expressions," Appl. Opt. **36**, 3165–3173 (1997).
9. F. E. Nicodemus, "Directional reflectance and emissivity of an opaque surface," Appl. Opt. **4**, 767–773 (1965).
10. B. P. Sandford and D. C. Robertson, Infrared reflectance properties of aircraft paints, U. S. Air Force Research Laboratory Preprint AFRL/VSBT ESC-94–1004, approved for public release August 1994.
11. W. C. Snyder, "Structured surface bidirectional reflectance distribution function reciprocity, theory and counterexamples," Appl. Opt. **41**, 4307–4313 (2002).
12. R. M. Watson and P. N. Raven, "Comparison of Measured BRDF Data with Parameterized Reflectance Models," Proc. SPIE **4370**, 159–168 (2001).
13. J. J. Koenderink and A. J. van Doorn, "Phenomenological description of bidirectional surface reflection," J. Opt. Soc. Am. A **15**, 2903–2912 (1998).
14. R. A. Brooks and G. D. Chiro, "Beam hardening in X-ray reconstruction tomography," Phys. Med. Biol. **21**, 390–398 (1976).
15. G. T. Herman, "Correction for beam hardening in computed tomography," Phys. Med. Biol. **24**, 81–106 (1979).
16. Z. Li, G. Hewei, L. Shuanglei, C. Zhiqiang, and X. Yuxiang, "Cupping artifacts analysis and correction for a FPD-based cone-beam CT, Proc. SPIE **6065**, 60650K (2006).
17. P. K. Kijewski and B. E. Bjarngard, "Correction for beam hardening in computed tomography," Med. Phys. **5**, 209–214 (1978).
18. R. E. Alverez and A. Macovski, "Energy-selective reconstructions in x-ray computerized tomography," Phys. Med. Biol. **21**, 733–744 (1976).
19. M. E. Davison and F. A. Grunbaum, "Tomographic reconstruction with arbitrary directions," Commun. Pure Appl. Math. **34**, 77–120 (1981).
20. A. K. Louis, "Picture reconstruction from projections in restricted range," Math. Meth. Appl. Sci. **2**, 209–220 (1980).

21. K. C. Tam, V. Perez-Mendez, and B. Macdonald, "Limited angle 3-D reconstructions from continuous and pinhole projections," IEEE Trans. Nucl. Sci. **27**, 445–458 (1980).
22. M. Ravichandran and F. C. Gouldin, "Reconstruction of smooth distributions from a limited number of projections," Appl. Opt. **27**, 4084–4097 (1988).
23. F. Natterer, *The Mathematics of Computerized Tomography* (Wiley, 1986), Chap. 6, pp. 160–166.
24. L. A. Shepp and B. F. Logan, "Reconstructing interior head tissue from x-ray transmissions," IEEE Trans. Nucl. Sci. **21**, 228–236 (1974).
25. Z.-P. Yang, L. Ci, J. A. Bur, S.-Y. Lin, and P. M. Ajayan, "Experimental observation of an extremely dark material made by a low-density nanotube array," Nano Lett. **8**, 446–451 (2008).
26. C. Srinivasan, "The blackest black material from carbon nanotubes," Curr. Sci. **94**, 974–975 (2008).
27. G. N. Ramachandran and A. V. Lakshminarayanan, "Three-dimensional reconstruction from radiographs and electron micrographs: application of convolutions instead of Fourier transforms," Proc. Natl. Acad. Sci. USA **68**, 2236–2240 (1971).
28. A. C. Kak and M. Slaney, *Principles of Computerized Tomographic Imaging* (IEEE, 1988).
29. R. L. Siddon, "Fast calculation of the exact radiological path for a three-dimensional CT array," Med. Phys. **12**, 252–255 (1985).
30. T. S. Trowbridge and K. P. Reitz, "Average irregularity representation of a rough surface for ray reflection," J. Opt. Soc. Am. **65**, 531–536 (1975).